Journal of Science: Advanced Materials and Devices 4 (2019) 483–491

Contents lists available at ScienceDirect

Journal of Science: Advanced Materials and Devices

journal homepage: www.elsevier.com/locate/jsamd

Original Article

Characterization and magnetic properties of hollow α-Fe_2O_3 microspheres obtained by sol gel and spray roasting methods

L. De Los Santos Valladares [a, b, c, *], A. Bustamante Domínguez [d], L. León Félix [d, e], J.B. Kargin [f], D.G. Mukhambetov [f, g], A.L. Kozlovskiy [h], N.O. Moreno [i], J. Flores Santibañez [d], R. Castellanos Cabrera [j], C.H.W. Barnes [c]

[a] Key Laboratory for Anisotropy and Texture of Materials (Ministry of Education), Northeastern University, Shenyang, Liaoning 110819, People's Republic of China
[b] Institute of Ceramics and Powder Metallurgy, School of Materials Science and Engineering, Northeastern University, Shenyang, Liaoning 110819, People's Republic of China
[c] Cavendish Laboratory, Department of Physics, University of Cambridge, J. J. Thomson Ave., Cambridge CB3 0HE, United Kingdom
[d] Laboratorio de Cerámicos y Nanomateriales, Facultad de Ciencias Físicas, Universidad Nacional Mayor de San Marcos, Ap. Postal 14-0149, Lima, Peru
[e] Laboratory of Magnetic Characterization, Instituto de Física, Universidade de Brasília, DF 70910-900 Brasília, Brazil
[f] Department of Technologies Commercialization, L.N. Gumilyov Eurasian National University, 010000 Astana, Kazakhstan
[g] Department of Information Systems, Almaty Academy of Economics and Statistics, 050035 Almaty, Kazakhstan
[h] Institute of Nuclear Physics, 010008 Astana, 2/1 Abylai-Khan Ave., Kazakhstan
[i] Departamento de Física, Universidade Federal de Sergipe, 49100-000 Sao Cristóvao, Sergipe, Brazil
[j] Laboratorio de Bioquímica, Facultad de Ciencias, Universidad Nacional Jorge Basadre Grohmann, Apartado Postal 316, Tacna, Peru

ARTICLE INFO

Article history:
Received 21 March 2019
Received in revised form
28 June 2019
Accepted 9 July 2019
Available online 31 July 2019

Keywords:
Hollow spheres
Hematite
Morin transition
Thermal hysteresis

ABSTRACT

In this work, we characterize the hollow hematite (α-Fe_2O_3) micro spheres obtained by two non-template techniques: i) sol gel and ii) spray roasting process. Both techniques allow the production of high yield hollow hematite spheres up to 100 g for the case of sol gel and up to 500 kg for the case of spray roaster process. The samples were characterized by X-ray diffraction, scanning electron microscopy and Mössbauer spectroscopy. The results indicate nearly uniform hollow spheres with diameters of around 1–1.5 μm and consisting of polycrystalline hematite. The Mössbauer spectroscopy reveals the signal change of quadrupole shift values evidencing the occurrence of the Morin transition and that the samples show an antiferromagnetic order at 77 K as in bulk hematite. The Morin temperature (T_M) for both samples was obtained from the measurements of the magnetic moments as a function of the temperature in zero field cooling (ZFC) and field cooling (FC) modes. The values of T_M for both samples are lower than that reported for bulk hematite ($T_{M(bulk)} = 263$ K). Remarkably, the ZFC and FC loops do not overlap in both samples, revealing irreversible Morin transition. However, the sample obtained by sol gel presents thermal hysteresis with T_M values of 260 K (in ZFC) and 248 K (FC). Whereas, the sample obtained by spray roaster process presents complete irreversibility and T_M values of 252 K (in ZFC) and 242 K (in FC).

1. Introduction

Hematite (α-Fe_2O_3) is the most stable iron oxide. It is *n*-type semiconductor ($E_g = 2.2$ eV) under ambient conditions and it is easy to synthesize. Due to its magnetic properties, corrosion-resistance, low cost and low toxicity it is widely used in catalysis [1–6], environmental protection [7–13], sensors [14–18], magnetic storage materials [19] and clinic diagnosis and treatment [20,21]. Hematite crystallizes in the rhombohedral primitive cell

* Corresponding author. Cavendish Laboratory, Department of Physics, University of Cambridge, J. J. Thomson Ave., Cambridge CB3 0HE, United Kingdom.
E-mail addresses: ld301@cam.ac.uk, luisdv@mail.neu.edu.cn (L. De Los Santos Valladares).

Peer review under responsibility of Vietnam National University, Hanoi.

https://doi.org/10.1016/j.jsamd.2019.07.004

isomorphous to that of ilmenite and corundum (hexagonal unit cell, space group $R\bar{3}c$) [22]. The primitive cell contains ten atoms (six Fe and four O) in contrast to only two atoms in simple transition-metal oxides with the rock salt structure [23].

In bulk α-Fe_2O_3 the spins are oriented along the [111] axis of the rhombohedral primitive cell [24] (along the [001] direction of the hexagonal unit cell [25]). It presents a first-order magnetic transition, called the Morin transition with the corresponding Morin temperature (T_M) = 263 K [26,27]. Below T_M, the two magnetic sublattices contain spins oriented antiparallel and the material is antiferromagnetic (AF). Between T_M and its Néel temperature ($T_N \approx 960$ K [28]) the spins lie in the basal {111} planes of the rhombohedral cell ({001} planes of the hexagonal unit) and they are slightly canted away (~1°) from the antiferromagnetic orientation, resulting in a "weak ferromagnetism" or "canted antiferromagnetic state" [29,30]. In general, T_M is dependent on many variables such as grain sizes [31], cation substitution [26,32,33], lattice defects (which generate internal strains) [34–37] and magnitude of the external magnetic field [38,39].

Regarding size, a small reduction in T_M is observed when the grain size decreases from 10,000 μm to 100 nm (~10 K) [39]. However, in the case of hematite nanoparticles, superparamagnetism is also expected together with an increase of magnetization in the weakly ferromagnetic state due to two contributions: the canted sublattices and the unpaired spins on the surface. In fact, T_M dramatically decreases for the particle sizes below 100 nm following a $1/D$ dependence [40]. For example, T_M is around 250 K for 100 nm-size-particles and 190 K for 30 nm-size-particles [39]. For particles with diameters of 2 to 8 nm, T_M is less than 4 K and it tends to disappear for smaller diameters [29,40–44]. The suppression of T_M in hematite nanoparticles is believed to be caused by high internal strains [35,36] and from small surface to volume ratio, which allows surface spins to dominate the magnetization [42].

To date, the preparation of a variety of hematite morphologies such as rhombohedra [45], particles [46–49], nanocubes [50,51], rings [52], wires [53,54], rods [55,56], fibbers [57], flakes [58], cages [59], airplane-like structures [60] and hierarchical structures [61–63] have been reported. On the other hand, the production of hollow microspheres of hematite is of current interest due to their promising applications in photonic crystals, encapsulation, drug delivery, catalysis, chemical storage, light fillers and low dielectric constant materials [45–63]. Some works have reported the production of crystalline hematite hollow spheres through various methods. However, most of the existing methods for obtaining the hematite hollow spheres involve templates, surfactants, toxic organic solvents, or complex steps [64]. Recently, we have obtained hematite hollow spheres by sol gel method [64,65] and spray roasting [66] techniques. In this paper, we compare the results of both techniques emphasizing in the study of their magnetic properties.

2. Experimental

2.1. Preparation of the samples by sol gel

The samples were prepared by two methods: sol–gel and spray roasting. The samples prepared by sol gel followed the same step reported in our previous work [64,65]. In brief, 200 ml of colloidal ferric nitrate nine-hydrate ($Fe(NO_3)_3 \cdot 9H_2O$) particles and mono hydrated citric acid ($C_6H_8O_7 \cdot H_2O$, 0.2 M) were dissolved in 800 ml of deionized water. The solution was vigorously agitated in a magnetic stirrer at 350 rpm (70 °C) for a period of 48 h to form $Fe(OH)_3$. The citric acid was used as ligand, to promote hydrolysis and to balance any difference of ions in the solution. A gel is formed by the hydrolysis of the ferric nitrate to iron oxyhydrate FeOOH polymer [67]. The gel was dried for two days at 40 °C to evaporate the acid, water residuals and other possible impurities formed during hydrolysis. This sample precursor was then introduced in a tubular furnace (LENTON LTF-PTF Model 16/610) for annealing in air at 600 °C. The furnace was programmed to increase the temperature at 2 ± 1 °C/min, to remain constant for 12 h, and finally to cool down at a rate of 2 ± 0.5 °C/min. This step has two purposes. First, to thermally oxidize the gel to obtain monophasic crystalline hematite; and secondly, to form bubble structures via boiling in air from which the hollow spheres are formed after quenching [64,65]. Remarkably, the solution precursor is stable in air and has a shelf life longer than two years. After reacting with water and following the same annealing process, similar hollow spheres can be obtained.

2.2. Preparation of the samples by the spray roasting process

The samples were obtained as secondary product of steel production described elsewhere [66,68,69]. This industrial technique can massively produce iron oxide particles [66,68–70]. In brief, thick layers of scale are formed on the surface of the steel strip during hot rolling. The cleaning of steel strips from the scale is carried out in two stages. Hot rolled strips pass before cold rolling through the scale-breaker where the main mass of scale exfoliates during the bend of the strip. Then scale residues on the steel strip surface are removed by passing a steel strip through an aqueous solution of hydrochloric acid. The iron oxides are dissolved in acid to form ferric chloride, $FeCl_2$. Then the spent pickling solution is fed in droplets through nozzles into a furnace with a temperature of 600 °C. Evaporation of water leads to a concentration gradient in the droplets. The $FeCl_2$ remaining in the droplet is enriched in the outer shell. When the concentration of $FeCl_2$ reaches 63.6 w-% in the shells, all $FeCl_2$ is bound in its hydrate form $FeCl_2 \cdot 4H_2O$. This creates a solid layer of reduced permeability on the outer surface of the droplet [68]. In the furnace, spray pyrolysis takes place, in which iron chloride decomposes into a dispersed oxide and hydrochloric acid vapor according to the pyrolysis reactions:

$$12FeCl_2 + 3O_2 \rightarrow 8FeCl_3 + 2Fe_2O_3\downarrow \quad (1)$$

$$2FeCl_3 + 3H_2O \rightarrow 6HCl\uparrow + Fe_2O_3\downarrow \quad (2)$$

Hydrochloric acid vapors are extracted from the top of the furnace and used for re-etching. The water remaining inside the cores causes swelling which changes the diameter of the solidified surface significantly. Eventually, the particle ends as hollow sphere of iron oxide settle on the bottom of the furnace and are pneumatically transported to the storage bin [66,68].

2.3. Measurements

The morphological analysis was performed using a scanning electron microscope (SEM–XL30 SFEG). With the help of the Image-J software, several SEM images have been used to count N ~1000 particles. Subsequently, a particle size histogram has been mounted using the Sturges method [71,72]. Phase formation and crystallization were analyzed by X-ray diffraction (XRD) using a universal diffractometer Bruker AXS D8 model FOCUS (Cu-Kα radiation). The step size is 0.02° per sec (2θ). Rietveld refinement was performed on the diffractograms by using the FullProf program (version 6.10, Nov. 2017) to estimate the cell parameters. The peak shapes were modeled with Thompson-Cox-Hasting pseudo-Voigt functions and the convergence of the fitting parameters to obtain a good fitting was controlled by observing the ratio R_{WP}/R_{EXP} (R-

weighted and R-expected ratio). In addition to the Rietveld refinement, the crystal parameters were also estimated by the Nelson–Taylor extrapolation and the average sizes of the crystallites are estimated from the main reflections of the XRD scans using the Scherrer equation [73] and neglecting peak broadening induced by residual stresses [73].

The Mössbauer measurements were performed with a conventional transmission Mössbauer spectrometer, operating with 1024 channels (after folding is 512 channels) and a Wissel INC. velocity module with a sinusoidal signal. The measurements were taken at room temperature (RT) and at 77 K. The obtained data were adjusted with the help of the program NORMOS generating a data file with the extension PLT and determining the difference between the experimental data and the calculated data. In this program, the good fitting is controlled by the value of the χ^2. The source employed was a ^{57}Co in rhodium matrix with 25 mCi. The isomer shift and the velocity scale were calibrated with respect to an α-Fe film at RT. The sample holder used has a diameter of 1 cm (0.7854 cm^2) which permitted to ascertain and quantify the small systematic effects of cosine smearing which usually occur in the folded Mössbauer spectra when relatively large collection solid angles are used. These conditions were appropriate to obtain a rating of 8500 counts per second.

The magnetic measurements were carried out in a DC magnetic property measurement system (DC-MPMS-SQUID) from Quantum Design. The temperature dependence of the magnetization data, $M(T)$, were taken in zero field cooling (ZFC) and field cooling (FC) modes under an external magnetic field of 1 kOe. The measurements were taken from 5 K to near room temperature (RT, 290 K) for the case of the sample obtained by sol gel and from 5 K to 400 K to the sample obtained by spray roasting. The field dependence of the magnetization data, $M(H)$, were taken under different applied magnetic fields (from −50 kOe to 50 kOe). The $M(H)$ data were corrected by removing the diamagnetic contribution of the sample holder. Since hematite's ferromagnetism is so weak and its demagnetizing field is around 10 Oe [74], any field contribution from internal demagnetization was neglected.

3. Results and discussions

Fig. 1 shows the scanning electron micrographs of the hollow spheres obtained by both techniques. Fig. 1(a) shows the morphology of the hollow spheres obtained by sol–gel. They are nearly uniform hollow spheres. The top left inset in Fig. 1(a) shows a broken sphere revealing its internal cavity. The broken sphere has an external diameter of around 2 μm and a shell thickness of less than 100 nm. The mean size of the spheres is around 1.60 μm as noted from the respective histogram (top right inset figure). In a previous work, we have noted that the surface of the spheres is rough since the shells are composed of different grains formed by 1–3 crystallites. Remarkably, by using this technique we have achieved up to 5 g of sample and we predict that it is possible to scale up to 1 kg since the ingredients and annealing process are cheap and the technique is highly reproducible [64,65]. For the sample obtained by the spray roasted process, Fig. 1(b) shows the micrograph of the hollow spheres. It is seen that part of the microspheres is broken which could be helpful to introduce loads for different applications. Note that different size spheres ranging from 10 to 100 μm are obtained. The estimated mean external diameter of the spheres is 76.6 μm as shown in the histogram inset in the figure. Similar to the previous case, the shells are aggregates of nanoparticles whose average size is about 50 nm. It is noteworthy that this industrial method allows to achieve up to 500 kg of hollow α-Fe_2O_3 microspheres.

Fig. 2(a) and (b) shows the X-ray diffraction patterns of the samples obtained by sol gel and spray roasting techniques, respectively. The hematite formation was identified for both samples from its main reflections (104) at 33.16°, (110) at 35.45° and its less intense peaks (113), (024), (116) and (300) (PDF2 card No. 86–550). Hematite has a rhombohedral centered hexagonal structure of corundum type (space group R–3C) with a close-packed oxygen lattice in which two-thirds of the octahedral sites are occupied by Fe(III) ions [75,76]. Rietveld refinement was performed to estimate the crystal parameters and atomic positions from the diffractograms of the hematite obtained by both techniques. The results are listed in Tables 1 and 2. Note that the parameters obtained for both samples are very similar. Remarkably, the crystallite size calculated for the hematite prepared by the sol gel technique is smaller than that for the sample obtained by spray roasting technique which has effect in the behavior of the Morin effect discussed below.

Fig. 3 shows the Mössbauer spectra (MS) of the hollow hematite microspheres obtained by sol gel and spray roasting fitted with the Lorentzian functions. The measurements were taken at room temperature and at 77 K. Table 3 lists the hyperfine parameters obtained after fitting the experimental data and resulting from the least-squares fitting. As it is shown in this table, the hyperfine parameters of both samples belong to the hematite phase. The room temperature Mössbauer spectra for both samples were fitted with only one sextet because the room temperature Mössbauer

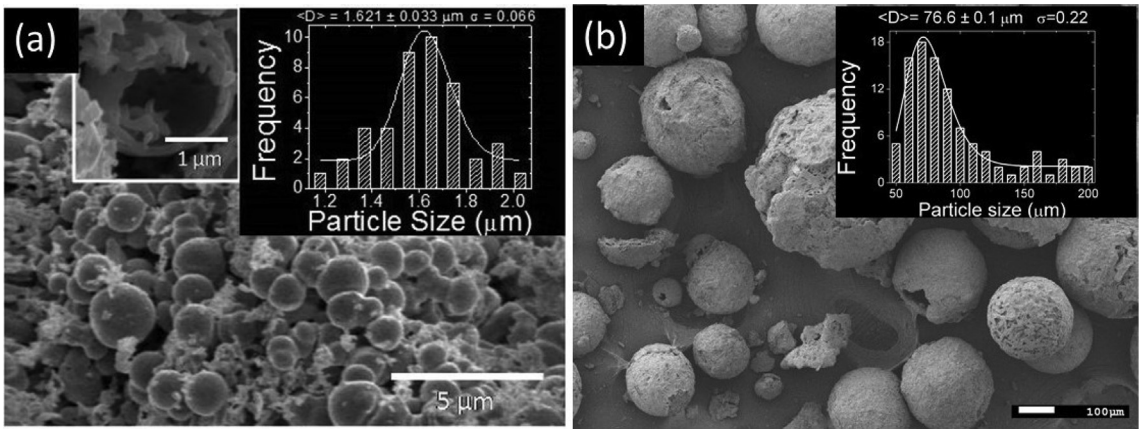

Fig. 1. Scanning electron microscope micrographs of the hollow spheres obtained by (a) sol-gel annealing and (b) spray roasting techniques. Top right inset in Fig. (a): Histogram giving a mean diameter of 1.60 μm. Top left inset in Fig. (a): A broken sphere revealing its internal cavity. Top right in Fig. (b): Histogram giving a mean diameter of 76.6 μm.

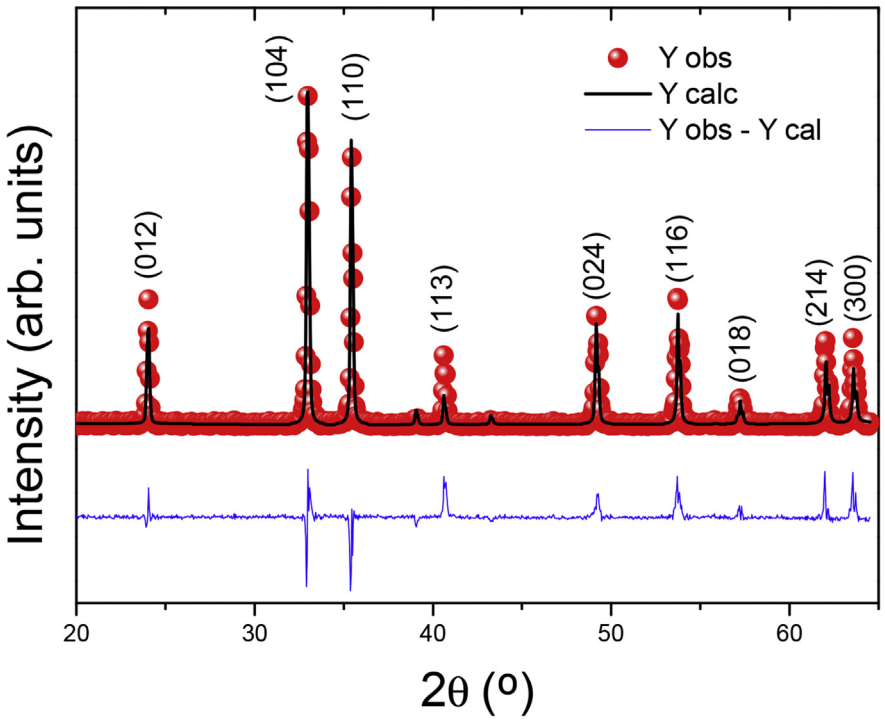

(a)

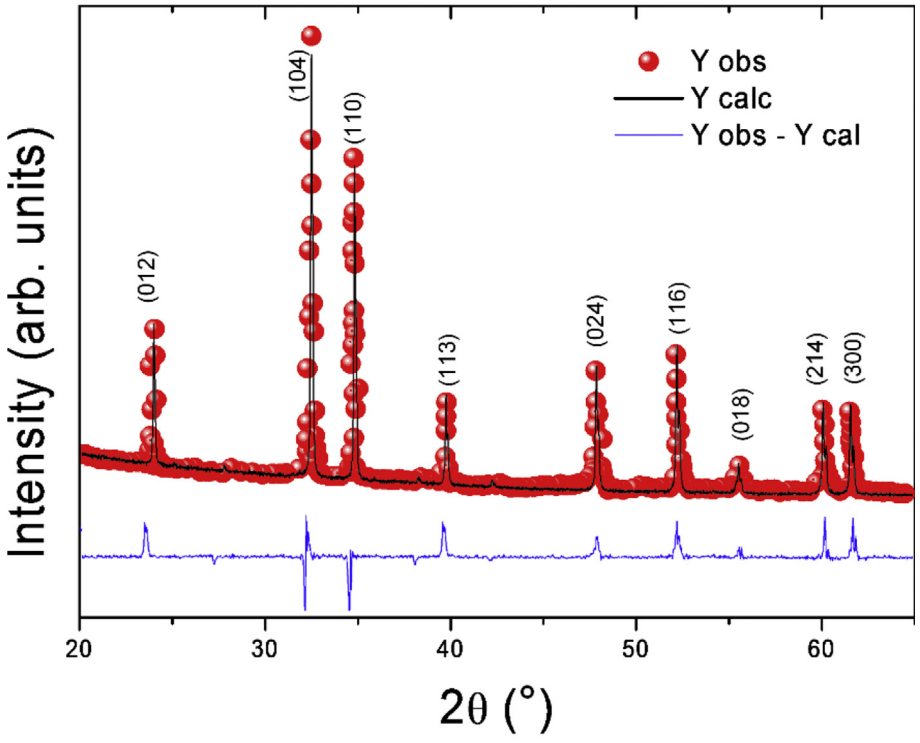

(b)

Fig. 2. X-ray diffraction patterns of the samples obtained by sol–gel annealing (a) and spray roasting techniques (b). Both techniques result in the formation of single phase hematite. Rietveld refinement was performed in the XRD of both samples and the differences between the observed and the calculated diffractograms are given as blue lines below each diffractogram.

Table 1
Crystallite size, lattice parameters and residual strains obtained by Rietveld refinements from XRD for the hematite phase.

Technique	⟨D⟩(nm)	$a = b$ (Å)	c (Å)	Density (g/cm^3)	R_{WP}/R_{Exp}
Sol gel	57.30	5.0641	13.8285	4.662	1.0
Spray roasting	88.02	5.0160	13.7448	4.662	1.0

Table 2
Crystal parameters and atomic positions for the hematite phase obtained in this work. Crystal structure: trigonal, space group: R−3c.

Preparation method	Atom	Wyckoff	Valence	X	y	Z	Occupancy
Sol gel	Fe	*C*	+3	0	0	0.35486	1
	O	*E*	−2	0.30936	0	0.25	1
Spray roasting	Fe	*C*	+3	0	0	0.35412	1
	O	*E*	−2	0.30943	0	0.26	1

spectrum for hematite shows only one sextet since there is only one crystalline site for Fe^{3+} in its hexagonal structure. This is in agreement with XRD patterns shown for each sample where no peaks other than those for the hematite phase of iron oxide are visible. The hyperfine magnetic field values are ascribed to the hematite phase since the quadrupole shift (2ε) values and the isomer shift (IS) values match well with the reported hyperfine values for hematite [77]. The negative values of the quadrupole shift are consistent with the weakly ferromagnetic (WF) phase, which are typical for bulk hematite [75]. Thus, the principal axis of the electric field gradient at the iron nucleus is along the [111] axis, perpendicular to the magnetic hyperfine field.

Table 3
Mössbauer parameters of hematite at room temperature and at 77 K.

Preparation method	T (K)	δ (mm/s)	2ε (mm/s)	B_{hf} (T)	Γ (mm/s)
Sol gel	300	0.37	−0.21	51.36	0.32
	77	0.47	0.41	53.4	0.28
Spray roasting	300	0.37	−0.20	51.32	0.31
	77	0.46	0.42	53.3	0.28

Description: δ = isomer shift relative to α-Fe (±0.01 mm/s), 2ε = quadrupole shift (±0.01 mm/s), B_{hf} = hyperfine magnetic field (±0.2 T) and Γ = line-width (±0.02 mm/s).

The MS taken at 77 K were also modeled with only one magnetic sextet. The quadrupole shifts, which are only slightly temperature dependent, change more drastically at Morin transition. At 77 K large positive values of 0.41 and 0.42 mm/s for 2ε are observed whereas the WF states have negative values of −0.21 and −0.20 mm/s at room temperature for the samples obtained by sol gel and spray roasting methods, respectively. Hence, the signal change of 2ε evidences the occurrence of the Morin transition (TM) and that the samples show antiferromagnetic order at 77 K as in bulk hematite. As the signal change of 2ε is determined for all of the synthesized samples, it confirms that the Morin transition occurs above 77 K for both samples what is in good agreement with the magnetic responses discussed below. It is worth mentioning that MS of the hollow α-Fe_2O_3 microspheres obtained by both methods were adjusted with one sextet belonging hematite phase and not with two sextets [78]. It may be due to the high crystalline nature of the samples so avoiding likely different atomic environments in microparticles of hematite.

Fig. 4 shows the magnetic response of the samples at different temperatures and applied magnetic fields. Fig. 4(a) shows the

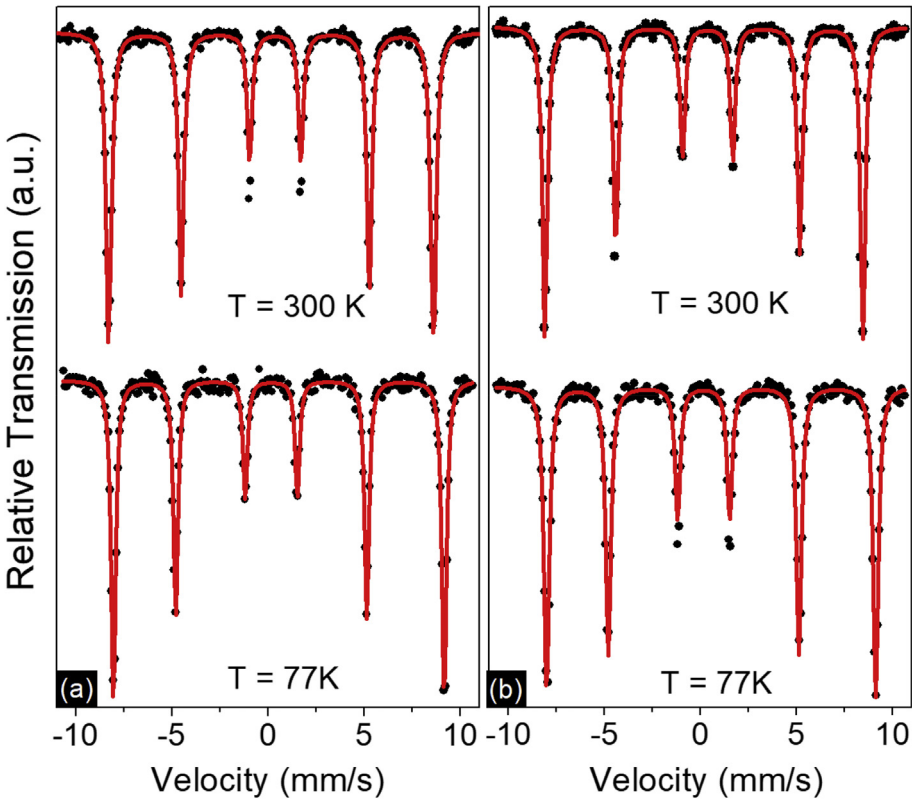

Fig. 3. Mössbauer spectra of the hollow hematite microspheres obtained by a) sol gel and b) spray roasting methods. The dots represent the measurement and the solid red lines correspond to the fit. The Mössbauer parameters are listed in Table 3.

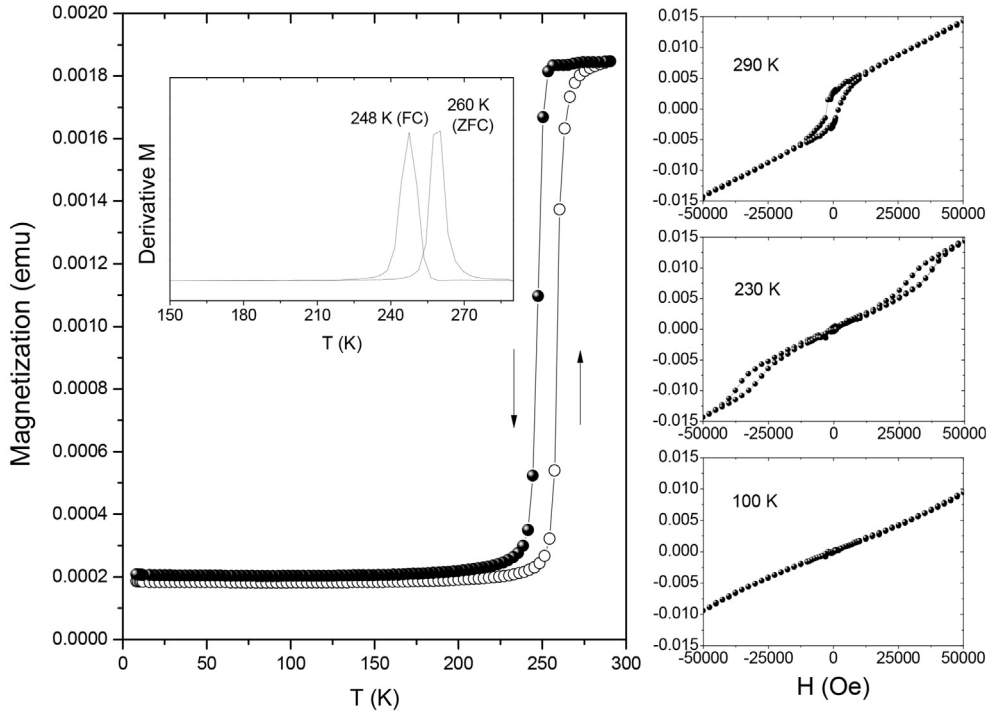

(a)

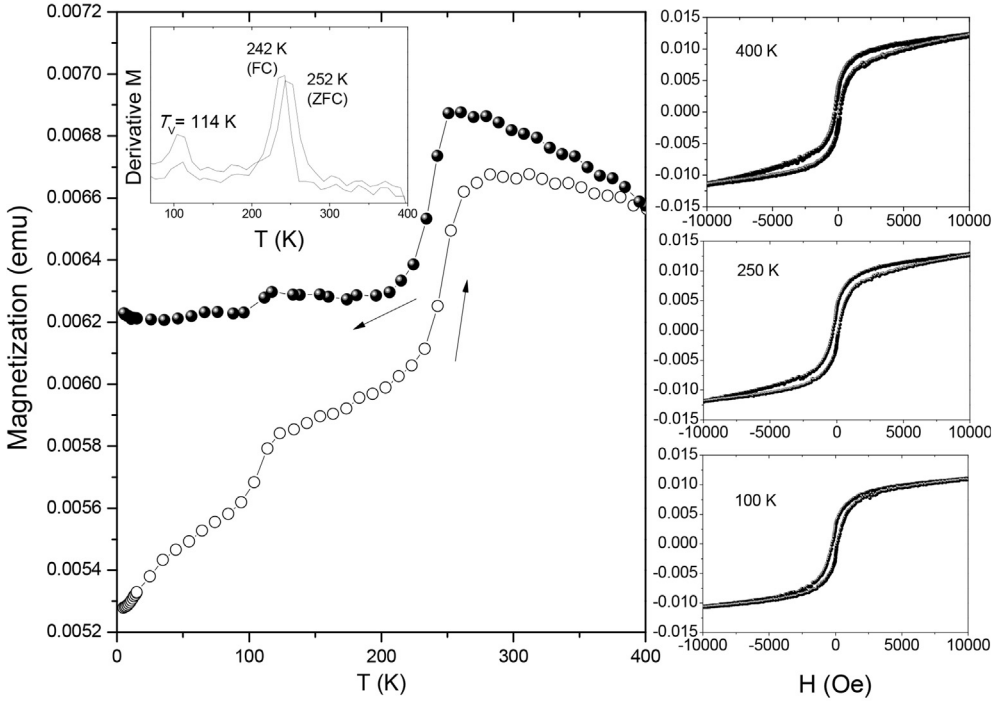

(b)

Fig. 4. Magnetic responses of the hematite samples obtained by a) sol gel annealing and b) spray roasting methods. The $M(T)$ loops were measured under an external magnetic field of 1 kOe. The $M(H)$ loops were measured at temperatures below, during and above the Morin transition, as indicated, for both samples.

dependence of the magnetization of the samples obtained by sol gel. The ZFC and FC loops in the $M(T)$ dependence plot clearly reveals the Morin transition, typical from the hematite phase. The T_M value was determined by the sharp peaks in the corresponding differential curves as they are indicated in the inset plots. Remarkably, the ZFC and FC loops do not overlap over a wide range

of temperatures, forming an observable thermal hysteresis in the whole temperature range, thus two T_M values (260 K from the ZFC loop and 248 K from the FC loop). This indicates that a certain degree of spins remains canted along the [111] direction along with the Morin transition.

Thermal hysteresis in hematite has been observed for many years mostly in thin films and submicron particles [36–40,79–84] than in bulk. Nevertheless, up to now, there is not a clear understanding about its origin because the exact mechanisms by which the Morin transition takes place into the hematite crystals remain elusive. Recently, Özdemir and Dunlop proposed that lattice defects could cause internal stresses which could anchor extensive regions of surface spins preventing spin rotation and thus resulting in thermal hysteresis [39]. It has also been proposed that rotation of the surface spins can cause nucleation centers that generate the transition throughout the entire crystal [30,83]. Furthermore, according to Frandsen et al. exchange coupling between particles is larger than dipole coupling in interacting hematite particles [25]. Exchange interaction between hematite particles suppresses superparamagnetic relaxation and produce spin rotation in the sublattices up to 15°, depending on particle size [85]. In this work, a difference between interacting spins oriented in-plane and out-plane the hematite crystallite causes a remnant magnetization upon thermal cycling (thermal hysteresis) due to some canted spins resisting to re-orientate in certain zones. These zones might locate in the crystallite boundaries forming the hollow hematite shells. In fact, in a previous work, we have found that the hollow spheres prepared by sol gel consist of multifaceted-polyhedron crystallites stuck together and forming the shells [64]. We believe that remanence zones are mainly located in the grain boundaries where interactions between randomly distributed Fe^{3+} moments do not lead to magnetic ordering. They might be also susceptible to the magnetic interactions among the nanocrystals.

The magnetization dependence of the hematite spheres obtained by the spray roasted process is given in Fig. 4(b). The $M(T)$ loop shows high irreversibility when measuring in the FC and ZFC modes. The loops do show frustrated Morin transitions without thermal hysteresis. The T_M values obtained by the peaks in the corresponding differential curves (inset plot) are 252 K for the ZFC loop and 242 K for the FC loop. Note that in contrast to the sample obtained by the sol gel annealing method, spray roasting produces less uniform and crystalline samples which might influence in a worse defined and high irreversible Morin effect as it has also observed by other authors [86,87]. In addition to this, the bumps around 120 K in the $M(T)$ loop for this sample reveal a Verwey transition. Verwey transition is the usual fingerprint to identify magnetite ($Fe^{3+}[Fe^{3+}Fe^{2+}]O_4$) [88–91], in which an ordering of Fe^{3+} and Fe^{2+} ions within the octahedral sites are thought to occur below the Verwey temperature (T_V). Thus, in the sample obtained by spray roasting method, hematite coexists with magnetite. In this sample, the amount of magnetite is too small to be detected by XRD and MS above, but by its magnetic properties in the SQUID-MPMS magnetometer. In contrast to the sample obtained by the sol gel, the presence of the magnetite in the sample obtained by spray roasting tends to increase the values of the magnetization to higher values and disturbing the antiferromagnetic behavior of the hematite. Similar to the value of T_M, T_V was also estimated from the differential curve of $M(T)$ (see inset plot), giving a value of 114 K.

The right plots in Fig. 4(a) show the magnetic dependences of the magnetization ($M(H)$) of the hematite sample obtained by the sol gel. The measurements were taken at three different temperatures around the Morin transition: 100, 230 and 290 K. The field dependence of the magnetization near RT (290 K) confirms the weak ferromagnetic state above T_M. At this temperature, magnetic saturation is reached at around $H_S \approx 20$ kOe. The ratio between the remanence magnetization (M_r) and the saturation magnetization (M_s) is $M_r/M_s \approx 0.81$. According to Özdemir and Dunlop, the values between 0.5 and 0.9 are typical from multidomain hematite particles [74]. Note that in our case, the shells are composed of multiple hematite grains and they should form interacting domains [64]. For the case of the hollow spheres obtained by the spray roaster method, the $M(H)$ loops on the right panels in Fig. 4(b) show clear hysteresis when measured at different temperatures. These are caused by the coexistence of magnetite and hematite in the sample. At 100 K the hysteresis loop presents 400 Oe coercivity field (H_c) and tends to decrease at higher temperatures (257 Oe at 250 K and 200 Oe at 400 K).

Remarkably, the sample obtained by sol gel presents a large coercive field (~2.7 kOe) at 290 K and it becomes zero as the temperature scales down. It is commonly accepted that large coercivity in bulk magnetic materials can be obtained by increasing either: (i) the resistance of domain rotation via increment of the magnetic anisotropy and (ii) the resistance of domain wall displacement via enhancing the distribution of internal stress and the volume concentration of impurity. However, up to date, there is no agreement of the exact causes for the coercivity increase in the case of hematite nanoparticles. It has been recently reported large H_c values near RT for particle diameters in the interval 120–450 nm (1.5–3.5 kOe) while for bigger sizes H_c tends to decrease exponentially [44]. The possibility of enhanced stress is discarded in this work since the samples were annealed at high temperatures which reduces the number of strains centeres. Similar to other works which relate the high coercivity values with the shape of the hematite particles and the amount of crystallites contained into them [92–94], we believe that the relative large coercivity obtained in this work might be associated to the shape and amount of the crystallites conforming the shells (2.6×10^3 [64]) which follow very well the correlation of coercivity values vs. number of composing crystallites reported by Rath et al. [94]. In other words, as in the thermal hysteresis reported above, the high coercivity obtained in this work should be caused by the large difference between domains alignment occurred into the crystallites and grain boundaries. As more polyhedron crystallites conform the shells, more grain boundaries and different spin alignments there are, thus resulting in a large coercivity.

At 230 K, for the case of the sol gel sample, a coexistence of antiferromagnetic and canted antiferromagnetic domains is detected. Note that the antiferromagnetic state is dominant at the lowest applied fields since there is a lack of remanence and coercivity. Irreversible hysteresis signals are obtained at higher magnetic fields than 30 kOe, enhancing the canted amount of spins (weekly ferromagnetism state). At 200 K, no remanence magnetization, nor coercivity, are obtained and the sigmoidal curve in the $M(H)$ loop reveals the complete antiferromagnetic state of the hematite hollow spheres.

4. Conclusion

We have successfully prepared hematite hollow spheres following the sol gel annealing and the spray roasting techniques. Both techniques allow us to obtain microspheres of hematite. The advantage of the sol gel technique is that the solution precursor has a shelf life longer than two years. The advantage of the spray roasted technique is that it allows the mass production of the hollow hematite spheres (up to 500 kg or even more). Hyperfine properties confirm the formation of hematite and that the Morin transition occurs above 77 K for the samples obtained by both methods. The magnetic measurements of the hollow hematite microspheres obtained by both techniques show the Morin behavior. For the sample obtained by sol gel, thermal hysteresis in

the $M(T)$ loops taken in ZFC and FC modes was obtained. The thermal hysteresis observed in the samples obtained by the sol gel might be caused by remanence zones located in the grain boundaries. Exchange interactions in these zones might also be responsible for generating the large coercivity observed in this work (~2.7 kOe) since as more crystallites conform the shells, more grain boundaries and different spin alignments there are. The samples obtained by the spray roasted technique show frustrated Morin behavior which comes from the presence of magnetite as a minor phase.

Acknowledgments

This work was supported by a grant from the Ministry of Education and Science of Kazakhstan on Science Development program (Agreement N°. 132 of March 12th, 2018).

References

[1] J.L. Zhang, Y. Wang, H. Ji, Y.G. Wei, N.Z. Wu, B.J. Zuo, Q.L. Wang, Magnetic nanocomposite catalyst with high activity and selectivity for selective hydrogenation of ortho-chloronitrobenzene, J. Catal. 229 (2005) 114.
[2] O. Shekhah, W. Ranke, A. Schule, G. Kolios, R. Schlogl, Styrene synthesis: high conversion over unpromoted iron oxide catalysis under practical working conditions, Angew. Chem. Int. Ed. 42 (2003) 5760.
[3] A.S.C. Brown, J.S.J. Hargreaves, B. Rijniersce, A study of the structural and catalytic effects of sulfation on iron oxide catalyst prepared from goethite and ferrihydrite precursors for methane oxidation, Catal. Lett. 53 (1998) 7.
[4] B.C. Faust, M.R. Hoffmann, D.W. Bahnemann, Photocatalytic oxidation of sulfur dioxide in aqueous suspensions of .alpha.-iron oxide (Fe_2O_3), J. Phys. Chem. 93 (1989) 6371.
[5] W. Weiss, D. Zscherpel, R. Schlogl, On the nature of the active site for the ethylbenzene dehydrogenation over iron oxide catalysts, Catal. Lett. 52 (1998) 215.
[6] T. Omori, H. Takahashi, H. Mametsuka, E. Suzuki, Photocatalytic oxygen evolution on α-Fe_2O_3 films using Fe^{3+} ion as a sacrificial oxidizing agent, Phys. Chem. Chem. Phys. 2 (2000) 3519.
[7] P. Li, D.E. Miser, S. Rabiei, R.T. Yadav, M.R. Hajaligo, The removal of carbon monoxide by iron oxide nanoparticles, Appl. Catal. B 43 (2003) 151.
[8] L.C.A. Oliveira, D.I. Petkowicz, A. Smaniotto, S.B.C. Pergher, Magnetic zeolites: a new adsorbent for removal of metallic contaminants from water, Water Res. 38 (2004) 3699.
[9] C.H. Lai, C.Y. Chen, Removal of metal ions and humic acid from water by iron-coated filter media, Chemosphere 44 (2001) 1177.
[10] M.S. Onyango, Y. Kojima, H. Matsuda, A. Ochieng, Adsorption kinetics of arsenic removal from groundwater by iron-modified zeolite, J. Chem. Eng. Jpn. 36 (2003) 1516.
[11] R.C. Wu, J.H. Qu, Y.S. Chen, Magnetic powder MnO-Fe_2O_3 composite-a novel material for the removal of the azo-dye from water, Water Res. 39 (2005) 630.
[12] R.C. Wu, H.H. Qu, H. He, Y.B. Yu, Removal of azo-dye Acid Red B(ARB)by adsorption and catalytic combustion using magnetic $CuFe_2O_4$ powder, Appl. Catal. B 48 (2004) 49.
[13] F. Herrera, A. Lopez, G. Mascolo, E. Albers, J. Kiwi, Catalytic combustion of Orange II on hematite: surface species responsible for the dye degradation, Appl. Catal. B 29 (2001) 147.
[14] J. Chen, L. Xu, W. Li, X. Gou, α-Fe_2O_3 nanotubes in gas sensor and lithium-ion battery applications, Adv. Mater. 17 (2005) 58.
[15] C.Z. Wu, P. Yin, X. Zhu, C.Z. OuYang, Y. Xie, J. Phys. Chem. B 110 (2006) 110.
[16] X.L. Gou, G.X. Wang, J. Park, H. Liu, J. Yang, Nanotechnology 19 (2008) 125606.
[17] J.S. Han, T. Bredow, D.E. Davey, A.B. Yu, D.E. Mulcahy, The effect of Al addition on the gas sensing properties of Fe_2O_3-based sensors, Sens. Actuators B 75 (2001) 18.
[18] E. Comini, V. Guidi, C. Frigeri, I. Ricco, G. Sberveglieri, CO sensing properties of titanium and iron oxide nanosized thin films, Sens. Actuators B 77 (2001) 16.
[19] H. Zeng, J. Li, J.P. Liu, Z.L. Wang, S.H. Sun, Exchange-coupled nanocomposite magnets by nanoparticle self-assembly, Nature 420 (2002) 95.
[20] A. Jordan, R. Scholz, K. Maier-Hauff, M. Johannsen, P. Wust, J. Nadobny, H. Schirra, H. Schmidt, S. Deger, S. Loening, W. Lanksch, R. Felix, Presentation of a new magnetic field therapy system for the treatment of human solid tumors with magnetic fluid hyperthermia, J. Magn. Magn. Mater. 225 (2001) 118.
[21] A.K. Gupta, M. Gupta, Synthesis and surface engineering of iron oxide nanoparticles for biomedical applications, Biomaterials 26 (2005) 3995.
[22] L. Pauling, S.B. Hendricks, J. Am, The crystal structures of hematite and corundum, Chem. Soc. 47 (1925) 781.
[23] G. Gollmann, A. Rohrbach, P. Entel, J. Hafner, First-principles calculation of the structure and magnetic phases of hematite, Phys. Rev. B 69 (2004) 165107.
[24] M.F. Hansen, C.B. Koch, S. Morup, Magnetic dynamics of weakly and strongly interacting hematite nanoparticles, Phys. Rev. B 62 (2000) 1124–1134.
[25] C. Frandsen, C.R.H. Bahl, B. Lebech, K. Lefmann, L.T. Kuhn, L. Keller, N.H. Andersen, M.v. Zimmermann, E. Johnson, S.N. Klausen, S. Morup, Oriented attachment and exchange coupling of α-Fe_2O_3 nanoparticles, Phys. Rev. B 72 (2005) 214406.
[26] F.J. Morin, Magnetic susceptibility of αFe_2O_3 and αFe_2O_3 with added titanium, Phys. Rev. 78 (1950) 819.
[27] C.G. Shull, W.A. Strauser, E.O. Wollan, Neutron diffraction by paramagnetic and antiferromagnetic substances, Phys. Rev. 83 (1951) 333.
[28] R.D. Zysler, M. Vasquez-Mansilla, C. Arciprete, M. Dimitrijewits, D. Rodríguez-Sierra, C. Saragovi, Structure and magnetic properties of thermally treated nanohematite, J. Magn. Magn. Mater. 224 (2001) 39–48.
[29] S.H. Gee, Y.K. Hong, J.C. Sur, D.W. Erickson, M.H. Park, F. Jeffers, Spin orientation of the hematite (α-Fe_2O_3) nanoparticles during the Morin transition, IEE Trans. Magn. 40 (2004) 2691–2693.
[30] H. Chow, F. Keffer, Soft surface magnons and the first-order magnetic phase transitions in antiferromagnetic hematite, Phys. Rev. B 10 (1974) 243.
[31] N. Amin, S. Arajs, Morin temperature of annealed submicronic α-Fe_2O_3 particles, Phys. Rev. B 35 (1987) 4810.
[32] N.A. Curry, G.B. Johnston, P.J. Besser, A.H. Morish, Neutron diffraction measurements on pure and doped synthetic hematite crystals, Philos. Mag. 12 (1965) 221–228.
[33] T. Ericsson, A. Krisnhamurthy, B.K. Srivastava, Morin-transition in Ti-substituted hematite: a Mossbauer study, Phys. Scr. 33 (1986) 88–90.
[34] S.A. Schetinkin, E. Wheeler, V.V. Kvardakov, M. Schlender, J. Baruchel, Observation of the phase coexistence in α-Fe_2O_3 at the Morin transition by synchrotron radiation white beam section topography, J. Phys. D Appl. Phys. 36 (2003) A118.
[35] D. Schoeer, R.C. Nininger, Morin transition in α-Fe_2O_3 microcyrstals, Phys. Rev. Lett. 19 (1967) 623–634.
[36] G.H. Muench, S. Arajs, E. Matijeviae, The morin transition in small α-Fe_2O_3 particles, Phys. Status Solidi A 92 (1985) 187–192.
[37] D.L. Williamson, E.L. Venturini, R.A. Graham, B. Morison, Morin transition of shock-modified hematite, Phys. Rev. B 34 (1986) 1899–1907.
[38] P.J. Besser, A.H. Morrish, Spin flopping in synthetic hematite crystals, Phys. Lett. 13 (1964) 289–290.
[39] Ö. Özdemir, D.J. Dunlop, Hysteresis and coercivity of hematite, Geochem. Geophys. Geosyst. 9 (2008) Q10Z01.
[40] R.D. Zysler, D. Fiorani, A.M. Tesla, L. Suber, E. Agnostinelli, M. Godinho, Size dependence of the spin-flop transition in hematite nanoparticles, Phys. Rev. B 68 (2003) 212408.
[41] J.L. Dromann, J.R. Cui, C.J. Sella, Mossbauer studies of Fe_2O_3 antiferromagnetic small particles, J. Appl. Phys. 57 (1985) 4283.
[42] W. Kundig, H. Bommel, G. Constabaris, R.H. Lindquist, Some properties of supported small α-Fe_2O_3 particles determined with the Mossbauer effect, Phys. Rev. 142 (1966) 327–333.
[43] C. Wu, P. Yin, C. Ou Yang, Y. Xie, Synthesis of hematite (α-Fe_2O_3) nanorods: diameter-size and shape effects on their applications in magnetism, lithium ion battery, and gas sensors, J. Phys. Chem. B 110 (2006) 17806.
[44] C.B. de Boer, T.A.T. Mullender, M.J. Dekkers, Low-temperature behaviour of haematite: susceptibility and magnetization increase on cycling through the Morin transition, Geophys. J. Int. 146 (2001) 201.
[45] T.J. Park, S.S. Wong, As-prepared single-crystalline hematite rhombohedra and subsequent conversion into monodisperse aggregates of magnetic nanocomposites of iron and magnetite, Chem. Mater. 18 (2006) 5289.
[46] Y.Y. Zhang, Q.J. Zheng, Quasicubic α-Fe_2O_3 nanoparticles with excellent catalytic performance, J. Phys. Chem. B 110 (2006) 3093.
[47] C.Q. Hu, Z.H. Gao, X.R. Yang, Facile synthesis of single crystalline α-Fe_2O_3 ellipsoidal nanoparticles and its catalytic performance for removal of carbon monoxide, Mater. Chem. Phys. 104 (2007) 429.
[48] S. Komarneni, R. Roy, Q.H. Li, Microwave-hydrothermal synthesis of ceramic powders, Mater. Res. Bull. 27 (1992) 1393.
[49] H. Katsuki, S.J. Komarneni, Microwave-hydrothermal synthesis of monodispersed nanophase α-Fe_2O_3, J. Am. Ceram. Soc. 84 (2001) 2313.
[50] S.B. Wang, Y.L. Min, S.H. Yu, Synthesis and magnetic properties of uniform hematite nanocubes, J. Phys. Chem. C 111 (2007) 3551.
[51] B. Hou, Y. Wu, L. Wu, Y. Shi, K. Zou, H. Gai, Hydrothermal synthesis of cubic ferric oxide particles, Mater. Lett. 60 (2006) 3188–3191.
[52] X.L. Hu, J.C. Yu, J.M. Gong, Q. Li, G.S. Li, α-Fe_2O_3 nanorings prepared by a microwave-assisted hydrothermal process and their sensing properties, Adv. Mater. 19 (2007) 2324.
[53] Y.L. Chueh, M.W. Lai, J.Q. Liang, L.J. Chou, Z.L. Wang, Systematic study of the growth of aligned arrays of α-Fe_2O_3 and Fe_3O_4 nanowires by a vapor-solid process, Adv. Funct. Mater. 16 (2006) 2243.
[54] X.G. Wen, S.H. Wang, Y. Ding, Z.L. Wang, S.H. Yang, Controlled growth of large-area, uniform, vertically aligned arrays of α-Fe_2O_3 nanobelts and nanowires, J. Phys. Chem. B 109 (2005) 215–220.
[55] J.J. Wu, Y.L. Lee, H.H. Chiang, D.K.P. Wong, Growth and magnetic properties of oriented α-Fe_2O_3 nanorods, J. Phys. Chem. B 110 (2006) 18108.
[56] L. Liu, H.Z. Kou, W.L. Mo, H.J. Liu, Y.Q. Wang, Surfactant-assisted synthesis of α-Fe_2O_3 nanotubes and nanrods with shape-dependent magnetic properties, J. Phys. Chem. B 110 (2006) 15218–15223.
[57] C.R. Gong, D.R. Chen, X.L. Jiao, Q.L. Wang, Continuous hollow α-Fe_2O_3 and α-Fe fibers prepared by the sol-gel method, J. Mater. Chem. 12 (2002) 1844.
[58] M.V. Reddy, T. Yu, C.H. Sow, Z.X. Shen, C.T. Lim, G.V.S. Rao, B.V.R. Chowdari, α-Fe_2O_3 nanoflakes as an anode material for Li-ion batteries, Adv. Funct. Mater. 17 (2007) 2792.

[59] D.B. Wang, C.X. Song, G.H. Gu, Z.S. Hu, Preparation of Fe_2O_3 microcages from the core/shell structures, Mater. Lett. 59 (2005) 782.
[60] S.Z. Li, H. Zhang, J.B. Wu, X.Y. Ma, S.R. Yang, Shape-control fabrication and characterization of the airplane-like FeO(OH) and Fe_2O_3 nanostructures, Cryst. Growth Des. 6 (2006) 351–353.
[61] S. W Cao, Y.J. Zhu, Hierarchically, nanostructured α-Fe_2O_3 hollow spheres: preparation, growth mechanism, photocatalytic property, and application in water treatment, J. Phys. Chem. C 112 (2008) 6253–6257.
[62] C. Jia, Y. Cheng, F. Bao, D.Q. Chen, Y.S. Wang, pH value-dependant growth of α-Fe_2O_3 hierarchical nanostructures, J. Cryst. Growth 294 (2006) 353–357.
[63] X.L. Hu, J.C. Yu, J.M. Gong, Fast production of self-assembled hierarchical α-Fe_2O_3 nanoarchitectures, J. Phys. Chem. C 111 (2007) 11180.
[64] L. De Los Santos Valladares, L. León Félix, S.M. Espinoza Suárez, A.G. Bustamante Domínguez, T. Mitrelias, S. Holmes, N.O. Moreno, J. Albino Aguiar, C.H.W. Barnes, Preparation and crystallization of hollow α-Fe_2O_3 microspheres following the gas-bubble template method, Mater. Chem. Phys. 169 (2016) 21–27.
[65] L. León, A. Bustamante, A. Osorio, G.S. Loarte, L. de los Santos Valladares, C.H.W. Barnes, Y. Majima, Synthesis and characterization of hollow α-Fe_2O_3 submicron spheres prepared by sol-gel, Hyperfine Interact. 202 (2011) 131–137.
[66] A. Agrawal, N. Naman, S.K. Dubey, Dynamics and control of a 4-dof wearable cable-driven upper arm exoskeleton, Int. J. Eng. Res. Rev. 2 (4) (2014) 70–73.
[67] D. Jagadeesan, U. Mansoori, P. Mandal, A. Sundaresan, M. Eswaramoorthy, Hollow spheres to nanocups: tuning the morphology and magnetic properties of single-crystalline α-Fe_2O_3, Angew. Chem. Int. Ed. 47 (2008) 7685–7688.
[68] M. Schiemann, S. Wirtz, Viktor Scherer, F. Bärhold, Spray roasting of iron chloride $FeCl_2$: laboratory scale experiments and a model for numerical simulation, Powder Technol. 228 (2012) 301–308.
[69] M.J. Ruthner, Process and Apparatus for Production of Ferric Oxide from Iron Chloride Solutions, United States Patent number 5,911,967, June 15th 1999.
[70] S.K. Sarna, Acid Regeneration for Spent Hydrochloric Pickle Liquor, Technical report, Sept 20th 2013. Available at, http://ispatguru.com/acid-regeneration-for-spent-hydrochloric-pickle-liquor/.
[71] F.H. Aragón, P.E. N de Souza, J.A.H. Coaquira, P. Hidalgo, D. Gouvêa, Spin-glass-like behavior of uncompensated surface spins in NiO nanoparticulated powder, Physica B 407 (2012) 2601.
[72] L. León-Félix, J. Chaker, M. Parise, J.A.H. Coaquira, L. De Los Santos Valladares, A. Bustamante, V.K. Garg, A.C. Oliveira, P.C. Moris, Synthesis and characterization of uncoated and gold-coated magnetite nanoparticles, Hyperfine Interact. 224 (2014) 179–188.
[73] B.D. Cullity, C.D. Graham, Introduction to Magnetic Materials, second ed., John Wiley and Sons, Inc., Publication, USA, 2009, pp. 48–66, pp. 115–149.
[74] Ö. Özdemir, D.J. Dunlop, Hysteresis and coercivity of hematite, J. Geophys. Res. Solid Earth 119 (2014) 2582–2594.
[75] R. Zboril, M. Mashlan, D. Petridis, Iron(III)oxides from thermal processes synthesis, structural and magnetic properties, Mossbauer spectroscopy characterization, and applications, Chem. Mater. 14 (2002) 969.
[76] X. Wang, X.Y. Chen, X.C. Ma, H.G. Zheng, M.R. Ji, Z. Zhang, Low-temperature synthesis of α-Fe_2O_3 nanoparticles with a closed cage structure, Chem. Phys. Lett. 384 (2004) 391.
[77] L.C. Sanchez, J.D. Arboleda, C. Saragovi, R.D. Zysler, C.A. Barrero, Magnetic and structural properties of pure hematite submitted to mechanical milling in air and ethanol, Physica B 389 (2007) 145–149.
[78] S. Music, I. Czakó-Nagy, I. Salaj-Obelic, N. Ljubešic, Formation of α-Fe_2O_3 particles in aqueous medium and their properties, Mater. Lett. 32 (1997) 301–305.
[79] P.J. Flanders, Spin axis rotation in hematite, J. Appl. Phys. 40 (1969) 1247–1248.
[80] V.G. Labushkin, N.N. Faleev, V.A. Figin, A.S. Tsaprilov, X-ray diffraction investigations of hematite single crystals. Phase transition from weakly ferromagnetic to pure antiferromagnetic, Sov. Phys. Solid State 18 (1976) 1658–1659.
[81] R.C. Nininger, D. Scroeer, Mossbauer studies of the Morin transition in bulk and microcrystalline α-Fe_2O_3, J. Phys. Chem. Solids 39 (1978) 137–144.
[82] K.B. Vlasov, E.A. Rozenberg, V.I. Timoshchuk, Y.G. Smorodinskii, Observation of a thermal hysteresis of the magnetization of a hematite single crystal near the Morin transition, Sov. Phys. Solid State 28 (1986) 1851–1853.
[83] G.F. Goya, M. Veith, R. Rapalavicuite, H. Shen, S. Mathur, Thermal hysteresis of spin reorientation at Morin transition in alkoxide derived hematite nanoparticles, Appl. Phys. A 80 (2005) 1523–1526.
[84] P.G. Bercoff, H.R. Bertorello, M.J. Oliva, Memory effect of ball-milled and annealed nanosized hematite, Physica B 398 (2007) 204–207.
[85] C. Frandsen, M. Morup, Spin rotation in α-Fe_2O_3 nanoparticles by interparticle interactions, Phys. Rev. Lett. 94 (2005) 027202.
[86] C. Luna, V. Vega, V.M. Prida, R. Mendoza-Reséndez, Morin transition in hematite nanocrystals self-assembled into three-dimensional structures, J. Nanosci. Nanotechnol. 12 (2012) 7571–7576.
[87] L. Suber, P. Imperatori, A. Mari, G. Marchegiani, M. Vasquez Mansilla, D. Fiorani, W.R. Plunkett, D. Rinaldi, C. Cannas, G. Ennas, D. Peddis, Thermal hysteresis of Morin transition in hematite particles, Phys. Chem. Chem. Phys. 12 (2010) 6984–6989.
[88] F. Walz, The Verwey transition-a topical review, J. Phys. Condens. Matter 14 (2002) R285–R340.
[89] E.J. Verwey, Electronic conduction of magnetite (Fe_3O_4) and its transition point at low temperatures, Nature 144 (1939) 327–328.
[90] A. Bhattacharjee, D. Roy, M. Roy, S. Chakraborty, A. De, J. Kusz, W. Hofmeister, Rod-like ferrites obtained through thermal degradation of a molecular ferrimagnet, J. Alloys Compd. 503 (2010) 449–453.
[91] P. Piekarz, K. Parlinski, A.M. Oles, Vibrational properties of alpha- and sigma-phase Fe-Cr alloy, Phys. Rev. B (2007) 165124–165139.
[92] H. Cao, G. Wang, J.H. Warner, A.A.R. Watt, Amino-acid-assisted synthesis and size-dependent magnetic behaviors of hematite nanocubes, Appl. Phys. Lett. 92 (2008) 013110.
[93] X.M. Liu, S.Y. Fu, H.M. Xiao, C.J. Huang, Preparation and characterization of shuttle-like α-Fe_2O_3 nanoparticles by supermolecular template, J. Solid State Chem. 178 (2005) 2798–2803.
[94] C. Rath, K.K. Sahu, S.D. Kulkarni, S. Anand, S. Anand, S.K. Date, R.P. Das, N.C. Mishra, Microstructure-dependent coercivity in monodispersed hematite particles, Appl. Phys. Lett. 75 (1999) 4171–4173.